Gholamrezaie, E., Scheck-Wenderoth, M., Cacace, M., Bott [Sippel], J., Heidbach, O., Bohnhoff, M., Strecker, M. R. (2021): Lithospheric strength variations and seismotectonic segmentation below the Sea of Marmara. - Tectonophysics, 815, 228999.

https://doi.org/10.1016/j.tecto.2021.228999

Lithospheric strength variations and seismotectonic segmentation below the Sea of Marmara

Ershad Gholamrezaie [a, b,*], Magdalena Scheck-Wenderoth [a, c], Mauro Cacace [a], Judith Bott [a], Oliver Heidbach [a], Marco Bohnhoff [a, d], Manfred R. Strecker [b]

[a] *Helmholtz Centre Potsdam–GFZ German Research Centre for Geosciences, Potsdam, Germany*
[b] *Institute of Geosciences, University of Potsdam, Germany*
[c] *Faculty of Georesources and Material Engineering, RWTH Aachen, Aachen, Germany*
[d] *Department of Earth Sciences, Freie University Berlin, Berlin, Germany*

Article info

Keywords:
North Anatolian Fault Zone
Sea of Marmara
Seismic gap
Lithospheric strength
Thermal modeling
Rheological modeling

Abstract

The Sea of Marmara is a tectonically active basin that straddles the North Anatolian Fault Zone (NAFZ), a major strike-slip fault that separates the Eurasian and Anatolian tectonic plates. The Main Marmara Fault (MMF), which is part of the NAFZ, contains an approximately 150 km long seismotectonic segment that has not ruptured since 1766. A key question for seismic hazard and risk assessment is whether or not the next rupture along this segment is likely to produce one major earthquake or a series of smaller earthquakes. Geomechanical characteristics such as along-strike variations in rock strength may provide an important control on seismotectonic segmentation. We find that variations in lithospheric strength throughout the Marmara region control the mechanical segmentation of the MMF and help explain its long-term seismotectonic segmentation. In particular, a strong crust that is mechanically coupled to the upper mantle spatially correlates with aseismic patches, where the MMF bends and changes its strike in response to the presence of high-density lower crustal bodies. Between the bends, mechanically weaker crustal domains that are decoupled from the mantle indicate a predominance of creeping. These results are highly relevant for the ongoing debate regarding the characteristics of the Marmara seismic gap, especially in view of the seismic hazard ($M_w > 7$) in the densely populated Marmara region.

1. Introduction

Unlike their marine counterparts, continental transform faults constitute complex areas of deformation that are often associated with rapidly changing lithospheric strength as well as variable widths and styles of deformation (*Sylvester*, 1988; *Stein et al.*, 1997; *Şengör et al.*, 2005; *Lockner et al.*, 2011; *Lindsey et al.*, 2014). One of the major problems in such regions is deciphering the extent, potential linkage of individual seismotectonic segments, rupture history and the relation- ships between creeping and rupturing segments (*Flerit et al.*, 2004; *Lindsey et al.*, 2014; *Bohnhoff et al.*, 2016b, 2017; *Khoshmanesh and Shirzaei*, 2018). Next to the San Andreas Fault the North Anatolian Fault Zone (NAFZ) is such a transform environment where pronounced changes in fault behavior and rock strength appear to be closely correlated (*Flerit et al.*,2004; *Şengör* et al., 2005; *Lockner et al.*, 2011; *Lindsey et al.*, 2014; *Bohnhoff et al.*, 2016b, 2017; *Khoshmanesh and Shirzaei*, 2018).

The NAFZ (Fig. 1a) is a right-lateral continental transform fault that extends from the Karliova triple junction in eastern Anatolia to the northern Aegean (*Şengör et al.*, 2005). The main drivers of plate motion along the NAFZ are the northward indentation of the Arabian plate in the east and back-arc spreading in the Aegean Sea due to the southward rollback of the Hellenic subduction zone in the west, which combine to produce a counterclockwise rotation of the Anatolian plate and a relative displacement rate of 25 mm yr^{-1} with respect to Eurasia (*Jackson and McKenzie*, 1988; *Flerit et al.*, 2004; Şengör et al., 2005). In the Marmara region in north-western Turkey, the NAFZ splits into three branches (Fig. 1b). About 80% of the relative displacement occurs at the northern branch that passes through the Sea of Marmara as the Main Marmara Fault (MMF; *Le Pichon et al.*, 2001), into the Gallipoli Penin- sula as the Ganos Fault, and then into the North Aegean Sea. In detail, the MMF consists of three main segments: (1) the Izmit bay segment between Izmit and the Tuzla bend, (2) the Princes' Island segment (PIS) between the Tuzla and Istanbul bends, and (3) the western-central segment between the Istanbul and Ganos bends (Fig. 1c).

The Marmara region has experienced a number of strong earth- quakes during the last few hundred years, indicating that the western- most portion of the NAFZ is a mature active fault, thus adding to the seismic hazard for the densely populated greater Istanbul metropolitan region (Fig. 1b and c). The 1999 Izmit (M_w 7.4) and Düzce (Mw 7.1) earthquakes were the most recent strong earthquakes in the Marmara region (*Bohnhoff et al.*, 2016b; *Yildirim and Tüysüz*, 2017). The Izmit event occurred at the easternmost tip of the Sea of Marmara and was the most recent of a sequence of strong, westward migrating earthquakes that have occurred along the NAFZ since 1939 (*Stein et al.*, 1997; *Armijo et al.*, 2002; *Lorenzo-Martín et al.*, 2006). Within this sequence, the MMF represents a seismic gap (Figs. 1 and 2) that has not ruptured since 1766 (*Bohnhoff et al.*, 2013). The western limit of this seismic gap is marked by the rupture of the 1912 M_w 7.4 Ganos earthquake (Figs. 1b and 2). Based on historic records, a recurrence interval of 250 years was suggested (*Ambraseys*, 2002; *Barka et al.*, 2002; *Parsons*, 2004; *Bohnhoff et al.*, 2013, 2016a, 2017; *Murru et al.*, 2016), suggesting that the MMF is mature and in its final stage of the seismic cycle.

* Corresponding author at: Section 4.5: Basin Modelling, Helmholtz Centre Potsdam–GFZ German Research Centre for Geosciences, Potsdam, Germany.
E-mail address: ershad@gfz-potsdam.de (E. Gholamrezaie).

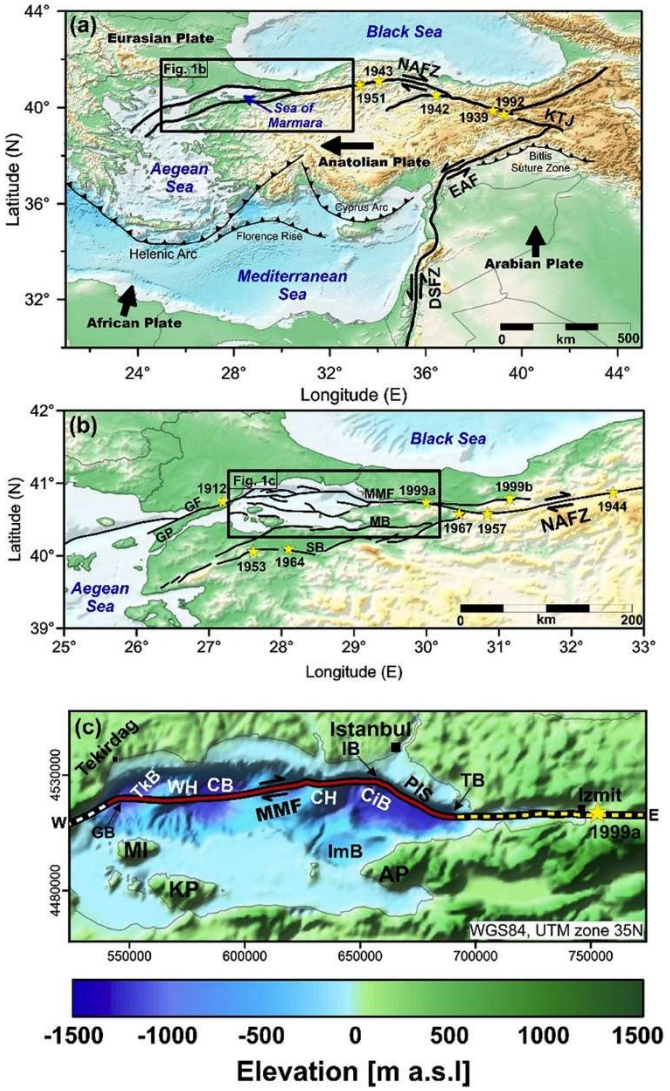

Figure 1. Location of the model area (after *Hergert et al.*, 2011 and *Gholamrezaie et al.*, 2019). (a) Tectonic map covering the contacts between the Arabian, African, Anatolian and Eurasian plates. Yellow stars show the epicenters of major earthquakes (Mw > 6.5) during the last century (*Stein et al.*, 1997; *Barka et al.*, 2002). (b) Westernmost sector of the NAFZ, showing the fault system (*Armijo et al.*, 2002, 2005). (c) Modeled area, showing the topography (*Le Pichon et al.*, 2001; *Amante and Eakins*, 2009), the seismic gap (red line) that has existed since 1766 (*Bohnhoff et al.*, 2013, 2017), and the approximate ruptures (*Barka et al.*, 2002; *Bohnhoff et al.*, 2017) related to the major events of 1912 Ganos (white dashed line) and 1999 Izmit (yellow dashed line). Abbreviations: North Anatolian Fault Zone (NAFZ), East Anatolian Fault (EAF), Dead Sea Fault Zone (DSFZ), Karliova triple junction (KTJ), Main Marmara Fault (MMF), middle branch (MB), southern branch (SB), Ganos Fault (GF), Gallipoli Peninsula (GP), Princes' Islands segment (PIS), Tuzla Bend (TB), Istanbul Bend (IB), Ganos Bend (GB), Çınarcık Basin (CiB), Central Basin (CB), Tekirdağ Basin (TkB), Imralı Basin (ImB), central high (CH), western high (WH), Marmara Island (MI), Kapidağ Peninsula (KP), and Armutlu Peninsula (AP). (For interpretation of the references to colour in this figure legend, the reader is referred to the web version of this article.)

A key question for seismic hazard and risk assessment in the region is whether the next rupture of the MMF will result in a single large earthquake, or in a number of smaller events due to geomechanical segmentation of the area (*Armijo et al.*, 2002, 2005; *Yaltirak*, 2002; *Le Pichon et al.*, 2003; *Hergert and Heidbach*, 2011; *Hergert et al.*, 2011; *Şengör et al.*, 2014; *Bulut et al.*, 2019; *Gholamrezaie et al.*, 2019). *Hergert and Heidbach* (2010) showed that changes in strike and dip of the MMF result in along-strike variations in stress loading, which sup- ports the hypothesis of a geomechanically controlled segmentation. However, they did not consider any depth variability of fault strength and considered a constant locking depth of 15 km. Furthermore, GPS observations (*Ergintav et al.*, 2014) are not conclusive as all recording stations are located on land and therefore too far away from the MMF along most of its length. Recent seafloor strain observations (*Lange et al.*, 2019; *Yamamoto et al.*, 2019) suggest that the seismic gap may include a complex system of locked and partially creeping fault segments with an accumulated slip deficit that has the potential to translate into an earthquake of M_w > 7.1. Nevertheless, it remains uncertain, which segments of the MMF are creeping and which ones are locked at a particular depth. Following these observations, we hypothesize that fault segmentation could be associated with variations in crustal rock strength, and hence with the background long-term rheo- logical conditions of the lithosphere adjacent to the MMF.

Understanding the structural setting of the Sea of Marmara and the interactions between the kinematics and geomechanics of the MMF is of key importance for seismic hazard and risk assessment. Geophysical observations and 3-D structural models both confirm the presence of crustal heterogeneities beneath the Sea of Marmara (*Laigle et al.*, 2008; *Bécel et al.*, 2009, 2010; *Bayrakci et al.*, 2013; *Kende et al.*, 2017; *Gholamrezaie et al.*, 2019). In particular, *Gholamrezaie et al.* (2019) identified lateral density heterogeneities within the crust on the basis of geophysical data integration and 3-D forward gravity modeling. Their results indicate that the variability in deformation patterns along the MMF may be due to the presence of two dome-shaped, high-density lower crustal bodies beneath the bends of the MMF (Fig. 2). This finding raised the question concerning the possible impact of such lithological heterogeneities beneath the Sea of Marmara on the overall lithospheric strength and earthquake characteristics. To address these topics, we used 3-D numerical modeling to estimate the long-term background strength of the lithosphere beneath the Marmara region based on a thermal-rheological model and assessed its influence on the MMF.

Our approach consists of modeling the yield strength of the litho- sphere beneath the Sea of Marmara. The yield strength is a measure of the maximum differential stress that a rock-type can sustain before it fails. It is generally temperature and pressure dependent and reflects the rheology of rocks at different depths. Variations in lithospheric yield strength at a particular location can be assessed using the concept of the yield strength envelope (YSE; *Goetze and Evans*, 1979). To characterize the YSE for the study area, we first describe the 3-D distribution of rock properties on the basis of structural geological models, which are then considered as input parameters to compute the 3-D lithospheric-scale thermal field. These results are subsequently used to calculate the 3-D distribution of the lithospheric strength in the Marmara region with the assumption of secondary creep as the main deformation mechanism. This methodology has been used previously at both global and regional scales to

investigate the long-term rheological characteristics of the lithosphere (*Tesauro et al.*, 2013; *Cacace and Scheck-Wenderoth*, 2016). We finally discuss how these results can be used to test our hypothesis that the segmentation of the MMF is mechanically controlled, where the presence of lithological heterogeneities causes significant variations in the active deformation modes along the MMF.

1.1. Structural setting and model configuration

Two contrasting tectonic settings have been proposed for the Sea of Marmara: (1) a purely extensional regime, which caused the opening of the Marmara basin and in which the MMF thereafter propagated within a weakened lithosphere as a single, strike-slip fault with a transtensional character along the Princes' Island segment (*Le Pichon et al.*, 2003, 2016), and (2) an a priori-transtensional regime formed by a releasing bend in the NAFZ (*Armijo et al.*, 2002, 2005) leading to the formation of the Sea of Marmara as a sequence of kinematically linked pull-apart basins. The bathymetric characteristics better agree with this latter setting since they reveal a subsidence pattern typical of a pull-apart basin with three main sub-basins along the MMF: the Çınarcık, Central, and Tekirdağ basins (Fig. 1c). These basins are separated by local structural highs: the central high and the western high. Below the seafloor two sedimentary successions separated by a regional unconformity (*Le Pichon et al.*, 2014) are preserved, documenting a change in the regional tectonic setting since the opening of the Sea of Marmara.

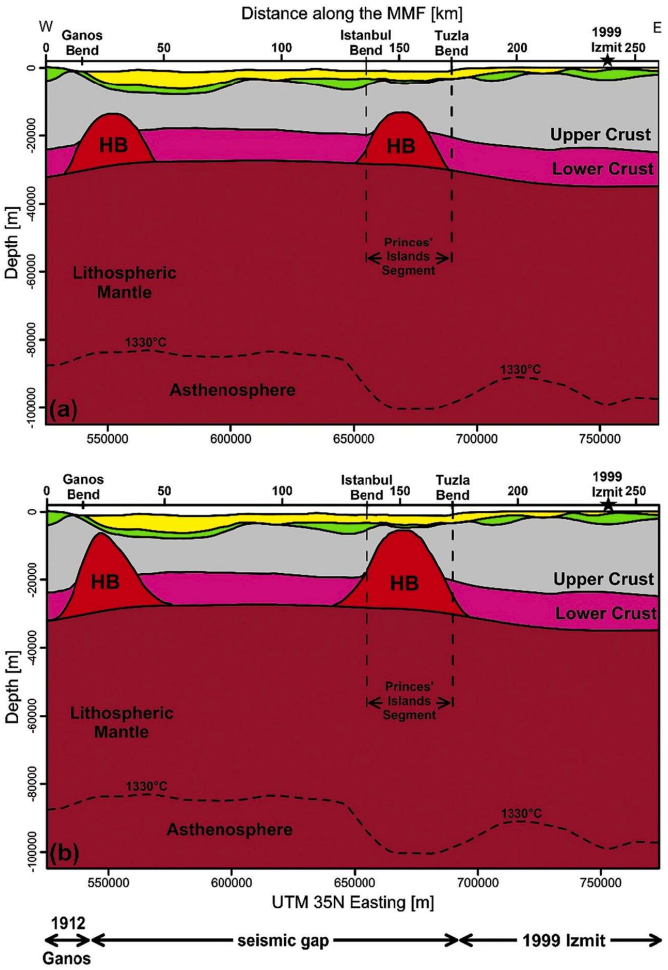

Figure 2. Cross-sections along the MMF from the two "end-member" structural model (*Gholamrezaie et al.*, 2019). (a) Model I, which includes two high-density bodies (HB) with an average density of 3150 kg m^{-3}, and (b) Model II, which also includes two high-density bodies but with an average density of 2890 kg m^{-3}. Yellow and green units represent synkinematic and pre-kinematic sediments, respectively. The black dashed line is the 1330°C isotherm, assumed as the thermal LAB and representing the position of the lower thermal boundary. The black star shows the epicenter of the 1999 Izmit earthquake (*Barka et al.*, 2002). 3-D structural model and corresponding average densities for different lithological units of Model I are stated in Fig. 3 and Table 1, respectively. 3-D structural model and related physical parameters of modeled geological units for Model II are also presented in the supplementary material (Fig. S3 and Table S1). (For interpretation of the references to colour in this figure legend, the reader is referred to the web version of this article.)

The geological units we consider in the 3D model are based on the integration of crustal-scale geophysical and geological data and con- strained by lithosphere-scale 3-D forward gravity modeling (*Gholamrezaie et al.*, 2019). As potential field modeling is inherently non- unique, *Gholamrezaie et al.* (2019) suggested two "end-member" structural models. These two models differ only in the density-geometry configuration of the crystalline crust while they are identical in their sediment and mantle configurations. Fig. 2 illustrates some of the main characteristics of these models. Although the presence of the high- density lower crustal bodies is required to fit the observed gravity, their exact shapes and densities may vary (Fig. 2). We therefore carried out all calculations for both end-member models. In the main text of this paper, however, we show the results of the thermal and rheological modeling for Model I (Fig. 2a), while the respective results for the sec- ond end-member model (Model II; Fig. 2b) are presented in the supplementary material. Details of the geological configuration are presented in Fig. 3 and Table 1 for Model I, and in the supplementary material (Fig. S3 and Table S1) for Model II.

The uppermost layers of the model consist of two sedimentary units (*Laigle et al.*, 2008; *Bécel et al.*, 2009, 2010; *Bayrakci et al.*, 2013; *Le Pichon et al.*, 2014; *Gholamrezaie et al.*, 2019). Of these, the upper siliciclastic unit, is syn-kinematic with the formation of the Sea of Marmara. It is therefore present only in the basin system, with thickness maxima largely coinciding with the present-day bathymetric sub-basins (Fig. 3). The lower sedimentary unit, consisting of alternating carbonates and siliciclastics, predates the opening of the Sea of Marmara. Accordingly, it is thinned beneath the present-day basin, but thicker in the surrounding onshore areas. Beneath these sedimentary units, seismic velocities (*Laigle et al.*, 2008; *Bécel et al.*, 2009, 2010; *Bayrakci et al.*, 2013) and modeled densities (*Kende et al.*, 2017; *Gholamrezaie et al.*, 2019) indicate the presence of a felsic upper crystalline crust that has been significantly thinned beneath the Sea of Marmara. This felsic unit is underlain by a lower, intermediate to mafic crystalline crust. Both the upper and lower crustal layers are cut by two dome- shaped, high-density bodies beneath the Çınarcık and Tekirdağ basins rising from the Moho to about 12 km depth b.s.l. (Figs. 2, 3 and 4a). Below the Moho (Fig. 3f), the topography of which is imaged by various seismological data (*Hergert and Heidbach*, 2010), a unit of lithospheric mantle follows down to the lithosphere-

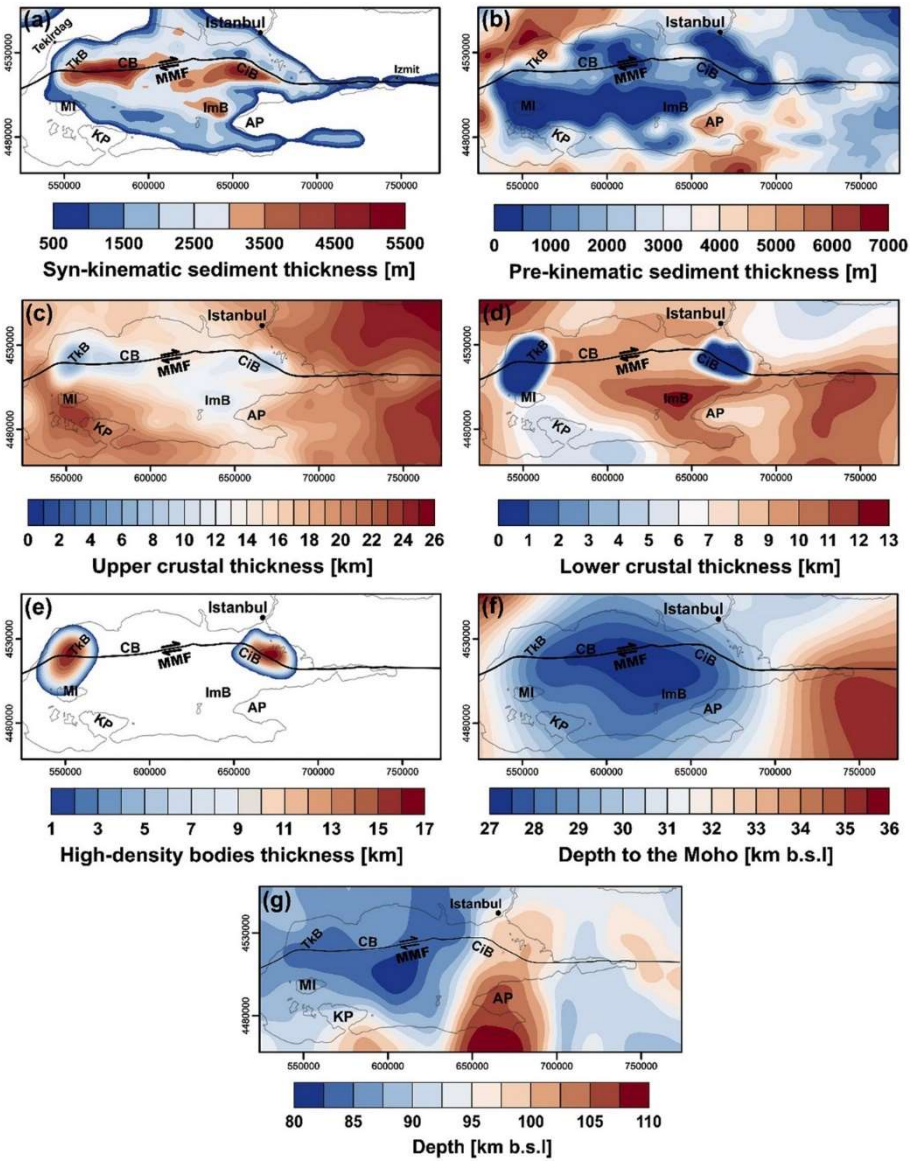

Figure 3. 3-D structural input for thermal and rheological modeling. (a) Syn-kinematic sediment thickness. (b) Pre-kinematic sediment thickness. (c) Upper crystalline crustal thickness. (d) Lower crystalline crustal thickness. (e) Thickness of the high-density bodies. (f) Depth to Moho. (g) Depth to thermal LAB (1330°C isotherm). Abbreviations: Main Marmara Fault (MMF), Çınarcık Basin (CiB), Central Basin (CB), Tekirdag˘ Basin (TkB), Imralı Basin (ImB), Marmara Island (MI), Kapidag˘ Peninsula (KP), and Armutlu Peninsula (AP).

asthenosphere boundary (LAB, Fig. 3g), which is defined based on seismic tomography (*Fichtner et al.*, 2013) and gravity modeling (*Gholamrezaie et al.*, 2019).

The lithological interpretations (Table 1) are derived from the observed P-wave velocities (*Laigle et al.*, 2008; *Bécel et al.*, 2009, 2010; *Bayrakci et al.*, 2013) and the densities modeled for each unit (*Gholamrezaie et al.*, 2019), together with compilations of laboratory measurements (*Christensen and Mooney*, 1995). However, the lithological interpretations for the high-density bodies are based only on their modeled densities as no deep seismic velocities are presently available. Consistent with these modeled densities, the high-density bodies have been interpreted as mafic granulites (Fig. 2, Table 1).

2. Methods

2.1. Thermal modeling

The thermal modeling was based on the general assumption that conduction is the main mechanism for heat transfer within the thermally equilibrated lithosphere. We solved the steady-state heat transport equation:

$$\Delta.(\Delta T) + S = 0 \qquad (1)$$

where S is the radiogenic heat production, λ is the thermal conductivity, ∇T is the temperature gradient. For the thermal modeling parametrization, constant values of average radiogenic heat production and average bulk (solid plus fluid) thermal conductivity were assigned to each geological unit (Table 1). These thermal properties were assigned considering the lithological interpretations from the 3-D density models (*Gholamrezaie et al.*, 2019) and corresponded to published values based on laboratory measurements (*Cermak and Rybach*, 1982; *Seipold*, 1992; *McKenzie et al.*, 2005; *Vilà et al.*, 2010).

Thermal boundary conditions were required to finalize the thermal model setup. The lateral boundaries were set to be insulating. For the upper thermal boundary condition, a constant value of 15°C was assigned to the topography-bathymetry surface (Fig. 1c). This value represents an average annual surface temperature in the Marmara region and agrees with the measured seafloor temperature in the Sea of Marmara (*Henry et al.*, 2007).

The lower thermal boundary condition was defined as the depth of the 1330°C isotherm (Figs. 3g and 4f) derived from modeled S-wave velocities (*Fichtner et al.*, 2013) using the *VeloDT* program (*Meeßen*, 2018), which is an implementation of the empirical approach of *Priestley and McKenzie* (2006). To define a lithospheric-scale model, the lower boundary condition was assumed to represent the thermal lithosphere-asthenosphere boundary (LAB). The material between the Moho and the lower boundary condition was therefore treated as homogeneous lithospheric mantle.

Finally, the heat transfer equation (Eq. (1)) was numerically solved in 3-D by using the Finite Element Method as implemented in the soft- ware Golem (*Cacace and Jacquey*, 2017; *Jacquey and Cacace*, 2017). The resolution of the model is 2500 m horizontally, that is identical to the input structural models (*Gholamrezaie et al.*, 2019). Regarding the vertical resolution, the properties are constant for each structural unit (Table 1). However, to ensure numerical stability and an appropriate aspect ratio of the finite elements, a mesh refinement was adopted (Table 1).

2.2. Rheological modeling

The rheological modeling was based on three main equations, these being for Byerlee's law (Eq. (2)), for power-law creep (Eq. (3)), and for Dorn's law creep (Eq. (4)):

$$\Delta\sigma_b = f_f \rho_b g z (1 - f_p) \tag{2}$$

$$\Delta\sigma_d = \left(\frac{\dot{\varepsilon}}{A}\right)^{\frac{1}{n}} exp\left(\frac{Q}{nRT}\right) \text{ if } \Delta\sigma < 200Mpa \tag{3}$$

$$\Delta\sigma_b = \sigma_0 \left(1 - \left[\frac{-RT}{Q_D} \ln \frac{\dot{\varepsilon}}{\dot{\varepsilon}_0}\right]^{\frac{1}{2}}\right) \text{ if } \Delta\sigma > 200Mpa \tag{4}$$

In the Byerlee's law (Eq. (2)), $\Delta\sigma_b$ is the brittle yield strength, f_f is the Byerlee's friction coefficient, ρ_b is the bulk density, g is the gravitational acceleration, z is the depth (below the ground surface) and f_p is the pore factor, which was considered to have a constant value of 0.37. In the creep equations (Eqs. (3) and (4)), $\Delta\sigma_d$ is the ductile strength, $\dot{\varepsilon}$ is the reference strain rate, A is the power-law strain rate, n is the power-law exponent, Q is the activation enthalpy, R is the gas constant (8.314 JL^{-1} mol^{-1}), T is the absolute temperature, σ_0 is Peierls' critical stress, QD is the Dorn's law activation energy, and $\dot{\varepsilon}_0$ is the Dorn's law critical strain rate.

According to Byerlee's law (Eq. (2)), the lithospheric brittle strength is essentially a temperature-independent

Table 1
Thermo-mechanical properties of the modeled geological units based on the interpreted lithologies and compilations of corresponding laboratory measurements.

Modeled geological unit	Syn-kinematic sediments	Pre-kinematic sediments	Upper crystalline crust	Lower crystalline crust	High-density bodies	Mantle (lithospheric)
Dominant lithology[a]	Clastic (poorly consolidated)	Clastic & chemical (consolidated)	Felsic (granite, gneiss)	Intermediate to mafic (gabbroic rocks)	Mafic (mafic granulite)	–
Average P-wave velocity[b] [m s^{-1}]	2250	4700	6000	6700	–	8000
Average bulk density[b] (ρ)[kg m^{-3}]	2000	2490	2720	2890	3150	3300
Bulk thermal conductivity (λ) [W m^{-1} K^{-1}]	2.00[c]	2.80[c]	3.00[d]	2.50[c]	2.00[d]	3.50[e]
Radiogenic heat production[f] (S) [μW m^{-3}]	1.00	0.50	3.10	0.25	0.15	0.01
Refinement	3	3	5	3	3	10
Reference rheological type	Brittle rocks	Brittle rocks	Granite dry[g]	Diabase dry[g]	Mafic granulite[h]	Olivine dry[i]
Activation enthalpy (Q) [kJ]	–	–	186	276	445	510
Power-law exponent (n)	–	–	3.30	3.05	4.20	3.00
Power-law strain rate (A) [Pa^{-n} s^{-1}]	–	–	3.16E-26	6.31E-20	8.83E-22	7.00E-14

[a] Christensen and Mooney (1995), [b]Gholamrezaie et al. (2019), [c]Cermak and Rybach (1982), [d]Seipold (1992), [e]McKenzie et al. (2005), [f]Vilà et al. (2010), [g]Carter and Tsenn (1987), [h]Wilks and Carter (1990), [i]Goetze and Evans (1979).

function of density and depth (*Byerlee*, 1978; *Ranalli*, 1995; *Burov*, 2011). At greater lithospheric depths, however, the dominant rheological behavior of rocks is non-nonlinear viscous flow, which is mainly temperature-dependent (*Karato and Wu*, 1993; *Burov*, 2011). Dorn's law has been shown to provide a better estimate of the solid-state creep in the lithospheric mantle (*Goetze*, 1978; *Goetze and Evans*, 1979). Dislocation creep in the crustal layers was therefore defined on the basis of the power-law (Eq. (3)) while creep in the lithospheric mantle was considered to be based on Dorn's law (Eq. (4)). The temperature variable for the strength calculations was derived from the modeled temperature distributions. We calculated the brittle strength with Byerlee's law, using the bulk densities from the 3-D density models (Table 1). The load of the seawater column ($\rho = 1025$ kg m^{-3}) was also considered as an initial pressure on the seabed. The Byerlee friction coefficient ranges between 0.6 and 0.85 for an extensional environment (Byerlee, 1978) and a constant average value of 0.75 was therefore used to model the brittle strength.

The reference strain rate ($\dot{\varepsilon}$ in Eqs. (3) and (4)) is the derivative of the strain function over time:

$$\dot{\varepsilon} = \frac{d}{dt}\varepsilon(t) = \frac{v(t)}{L_0} \tag{5}$$

where $\varepsilon(t)$ is the strain change over the time, $v(t)$ is the speed (slip rate), and L_0 is the original length (i.e., the width of the modeled area). By considering the entire 100 km width of the modeled area and using a slip rate for the MMF (*Le Pichon et al.*, 2003; *Flerit et al.*, 2004; *Reilinger et al.*, 2006; *Hergert and Heidbach*, 2010) of 12.8–24.8 mm yr^{-1}, the average reference strain rate calculated for the modeled area was about 10^{-14} s^{-1}.

The mechanical parameters assigned to the structural units were chosen on the basis of the interpreted physical properties of the modeled units and laboratory measurements on their reference rheological equivalents (Table 1). For the calculation of glide creep in the lithospheric mantle, the values of the Dorn's law rheological parameters were considered to be constant values (8.5 x 10^9 Pa for the Peierls' critical stress, 5.7 x 10^{11} s^{-1} for the critical strain rate, and 535 kJ mol^{-1} for the activation energy; Burov, 2011).

In order to visualize the rheological modeling results, the YSE was calculated as a minimum function of the brittle and ductile strengths (Eq. (6)). We also vertically integrated the modeled strength over the entire thickness of the lithosphere and crust (Eq. (7)), and calculated the ratio between the integrated crustal strength and the total lithospheric strength.

$$YSE = \min(\Delta\sigma_b \Delta\sigma_d) \tag{6}$$

$$\sigma(z) = \int_{z_0}^{z_1} \min(\Delta\sigma_b \Delta\sigma_d)\, dz \tag{7}$$

Within the crustal domain, the effective viscosity (η_{eff}) can be parameterized based on the thermally activated power-law dislocation creep (*Ranalli*, 1995). Accordingly, the efficiency of viscous creep in Fig. 8 was calculated based on the following equation:

$$n_{eff} = \frac{2^{\frac{1-n}{n}}}{3^{\frac{1+n}{2n}}} A^{\left(-\frac{1}{n}\right)} \dot{\varepsilon}^{\left(\frac{1}{n}-1\right)} exp\left(\frac{Q}{nRT}\right) \tag{8}$$

We used a C++ script, based on the previous work of *Cacace and Scheck-Wenderoth* (2016), to numerically calculate the lithospheric strength and to obtain the related results.

3. Results

3.1. The thermal field

The 3-D conductive thermal field was calculated (see Methods) based on the structural model (Fig. 3) and corresponding thermal properties (Table 1). Fig. 4 illustrates the main characteristics of the modeled thermal field using the depth to the 450°C and 750°C isotherms, as well as lateral temperature variations at the Moho and the depth to the thermal LAB (1330°C isotherm). To facilitate the interpretation of the thermal field derived from the structural model, the depth to the top of the high-density bodies and the Moho topography are also shown in Fig. 4a and c, respectively. Additional temperature-depth maps can be found in the supplementary material (Fig. S1).

The 450°C isotherm is often used as a proxy to define the effective elastic thickness of the lithosphere since it corresponds to the temperature at which felsic crustal rocks start to deform by creep (*Braun et al.*, 2013). The modeled 450°C isotherm (Fig. 4b) is shallowest in the eastern part of the analyzed area (~13 km b.s.l.) and deepest beneath the Sea of Marmara. In particular, it is deepest (~18 km b.s.l.) beneath the Çınarcık and Tekirdağ basins. These locations spatially correlate with the high-density bodies, which indicates that these bodies represent colder environments than their surrounding crystalline crustal rocks.

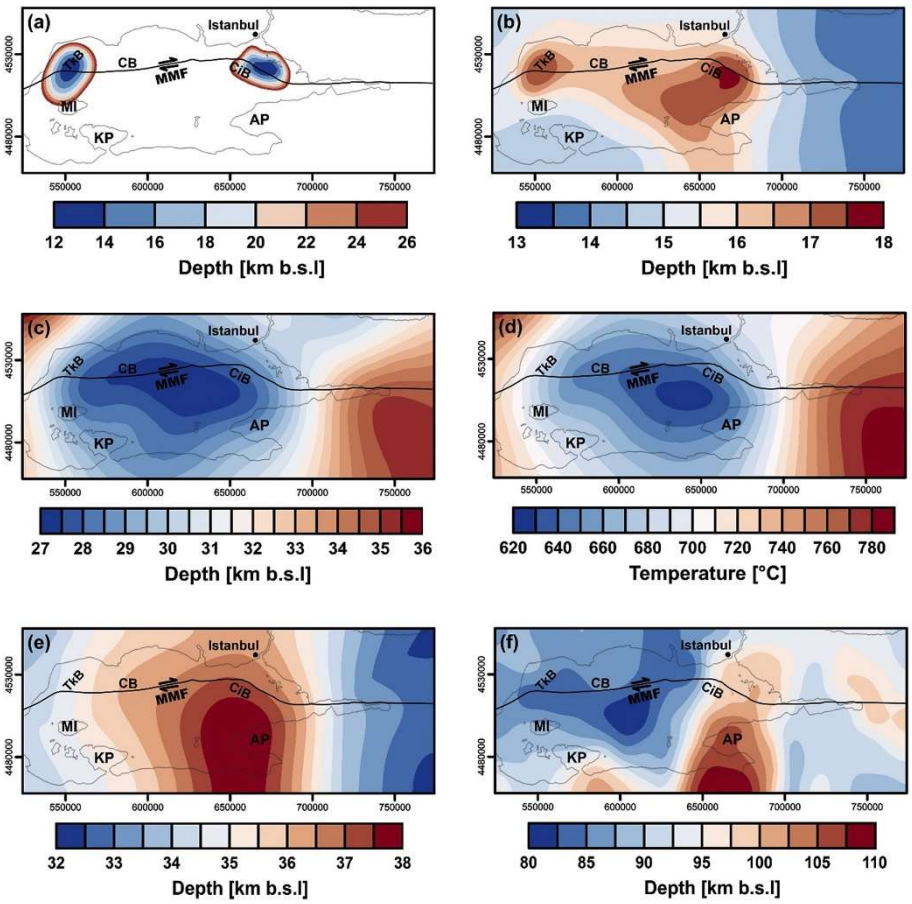

Figure 4. Crustal geometry and results of thermal modeling. (a) Depth to the high-density bodies. (b) Depth of the modeled 450°C isotherm. (c) Depth to the Moho. (d) Temperature distribution map on the Moho. (e) Depth of the modeled 750 ◦ C isotherm. (f) Depth to the thermal LAB which is assigned as the lower thermal boundary (1330 ◦ C). Abbreviations: Main Marmara Fault (MMF), Çınarcık Basin (CiB), Central Basin (CB), Tekirda˘g Basin (TkB), Marmara Island (MI), Kapida˘g Peninsula (KP), and Armutlu Peninsula (AP).

Comparing the depth variations of the 450°C isotherm with the Moho topography reveals that the crustal thickness exerts a major control on the deep crustal thermal field. Specifically, the lateral thickness variations of upper crystalline crust, and respectively the presence of a thicker felsic upper crystalline crust (Fig. 3c) enriched in heat-producing elements (Table 1) results in higher temperatures (Fig. 4, and Fig. S1 in the supplementary material). This influence on the deep thermal field is also expressed in the modeled temperature distribution at the Moho (Fig. 4d); here, maximum temperatures (up to 790°C) are modeled where the Moho is deepest and the upper crystalline crust is thickest in the eastern part of the study area. In contrast, the lowest Moho temperatures (~620°C) are modeled beneath the Sea of Marmara, where the crust has been thinned and the Moho is shallowest.

The depth to the 750°C isotherm (Fig. 4e) illustrates the lateral temperature distribution in the upper parts of the lithospheric mantle below the study area. In general, this isotherm is deeper beneath the Sea of Marmara compared to the surrounding onshore areas. This indicates that the upper parts of the lithospheric mantle are colder beneath the Sea of Marmara than below its surroundings.

Overall, the lack of a clear spatial correlation between the depth of the thermal LAB (Fig. 4f) and the crustal thermal field indicates that the crustal setting beneath the Marmara region ultimately dominates the thermal configuration. Deeper than approximately 50 km b.s.l, however, the depth of the thermal LAB, imposed as the lower thermal boundary condition (see Methods), controls the lateral variations in temperature (Fig. S1 in the supplementary material).

3.2. Integrated lithospheric strength

The results of the rheological modeling reveal variations in the integrated lithospheric and crustal strengths (Fig. 5). The lithosphere strength is low towards the Anatolian Plateau in the eastern part of the modeled area, and increases beneath the Sea of Marmara (Fig. 5a). This pattern of variation in lithospheric strength has no clear spatial correlation with the depth to the thermal LAB (Fig. 4f). Instead, it correlates with the temperature distribution at the Moho (Fig. 4d): where the Moho surface is relatively shallow the lithospheric strength tends to be high, and vice versa.

The crustal strength (Fig. 5b) is low where the upper crystalline crust is thick (Fig. 3c). As a thicker felsic crust produces more radiogenic heat (*Vilà et al.*, 2010), this results in a hotter and mechanically weaker crust in comparison to

areas where the upper crust thins out (Figs. 3 and 4, and Fig. S1 in the supplementary material). The integrated crustal strength reaches its highest values at the locations of the high-density bodies. Accordingly, the ratio of the integrated crustal strength to total lithospheric strength is highest at these locations (Fig. 5c). This indicates that the high-density bodies are the main crustal contributor to the long-term integrated lithospheric strength in the offshore area and along the MMF.

3.3. Thermal and rheological characteristics along the MMF

The results derived from our thermal-rheological modeling are illustrated along a profile which coincides with the orientation of the MMF (Fig. 6). The structural model (Fig. 6a) is also shown together with the observed seismicity (*GEOFON Data Centre*, 1993; *Wollin et al.*, 2018), the depth of the 450°C and 750°C isotherms, as well as the calculated YSEs at four different locations (Fig. 6b). Furthermore, variations in integrated lithospheric and crustal strengths (Fig. 6c) as well as their ratio (Fig. 6d) are also illustrated.

The lower crust is a weak ductile sector along the central part of the MMF, while the upper few kilometers of the lithospheric mantle are relatively strong (Fig. 6b). This indicates a "jelly-sandwich" rheological configuration (*Burov and Watts*, 2006; *Burov*, 2011) along the MMF, characterized by a strong upper crystalline crust that is mechanically decoupled from a strong lithospheric mantle by a relatively weak lower crystalline crust. However, this mechanical configuration does not apply to those areas, where the high-density bodies are located and which constitute major local rheological heterogeneities. At these locations, the modeled YSE suggests a rather strong crust that is mechanically coupled with the underlying mantle.

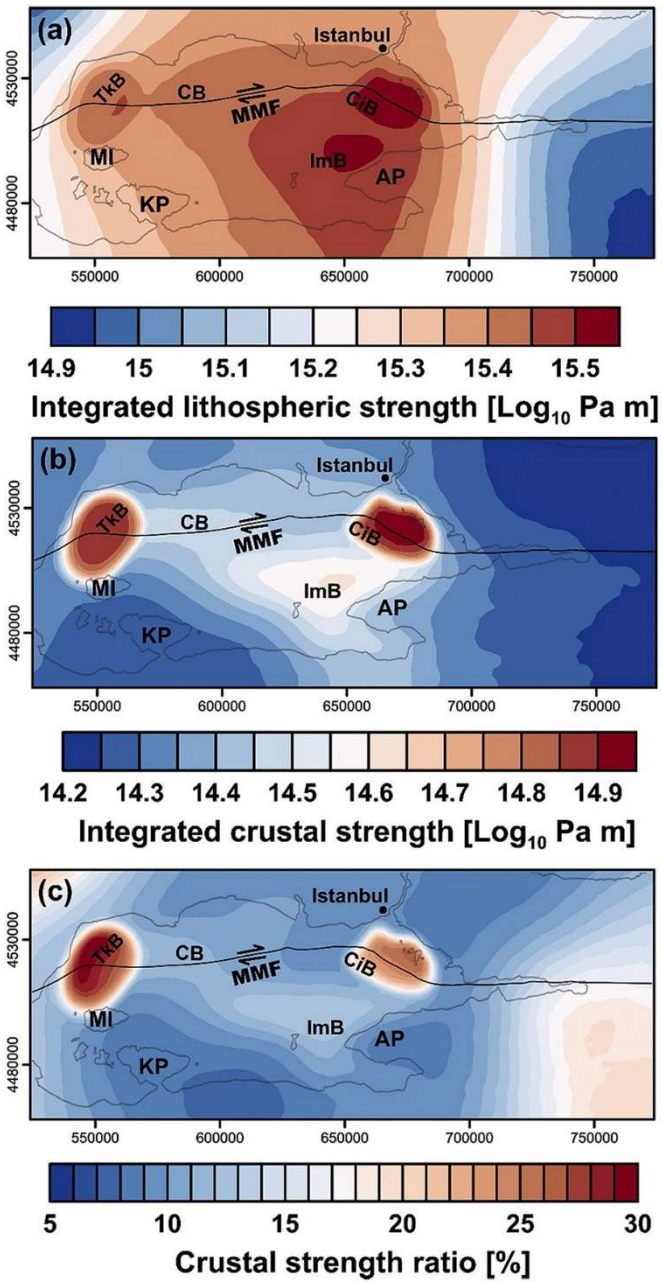

Figure 5. Modeled lithospheric strength. (a) Integrated lithospheric strength. (b) Integrated crustal strength. (c) Ratio of the integrated crustal strength to the total integrated lithospheric strength. Abbreviations: Main Marmara Fault (MMF), Çınarcık Basin (CiB), Central Basin (CB), Tekirdağ Basin (TkB), Imralı Basin (ImB), Marmara Island (MI), Kapidağ Peninsula (KP), and Armutlu Peninsula (AP).

4. Discussion

Our results indicate that modeled lateral variations in lithospheric strength in the Marmara region correlate with crustal compositional heterogeneities rather than with thermal anomalies within the mantle. The spatial correlation between the mechanically strong high-density bodies and bends in the MMF suggests that these crustal rheological contrasts may have influenced the kinematics of the fault. In addition, as the observed aseismic patches along the MMF (*Wollin et al.*, 2018) spatially correlate with the presence of a mechanically strong crust, the realms of the two high-density bodies may exemplify the locked segments of the MMF. Accordingly, our findings support the hypothesis that the observed segmentation along the MMF is controlled by the presence of a mechanically hetero-geneous off-fault crustal configuration.

To assess the thermal structure and strength of the lithosphere beneath the Sea of Marmara, the structural setting was derived from density models that integrated various geological and geophysical datasets and was additionally constrained by 3-D forward gravity modeling (*Gholamrezaie et al.*, 2019). The depth to the Moho discontinuity in the structural models had been obtained by interpolating between various seismological observations (*Hergert et al.*, 2011). *Gholamrezaie et al.* (2019) showed that the Moho topography is consistent with observed gravity, and their density model could ultimately resolve the free-air anomalies by considering lateral crustal density heterogeneities (dome-shaped, high-density bodies; Fig. 2). Accordingly, the wavelength of the residual anomalies of their model did not indicate density heterogeneities below the Moho discontinuity. However, given the geodynamic setting of the last million years in the Sea of Marmara, the upper lithospheric mantle might not be as homogeneous as considered in our model settings. In addition,

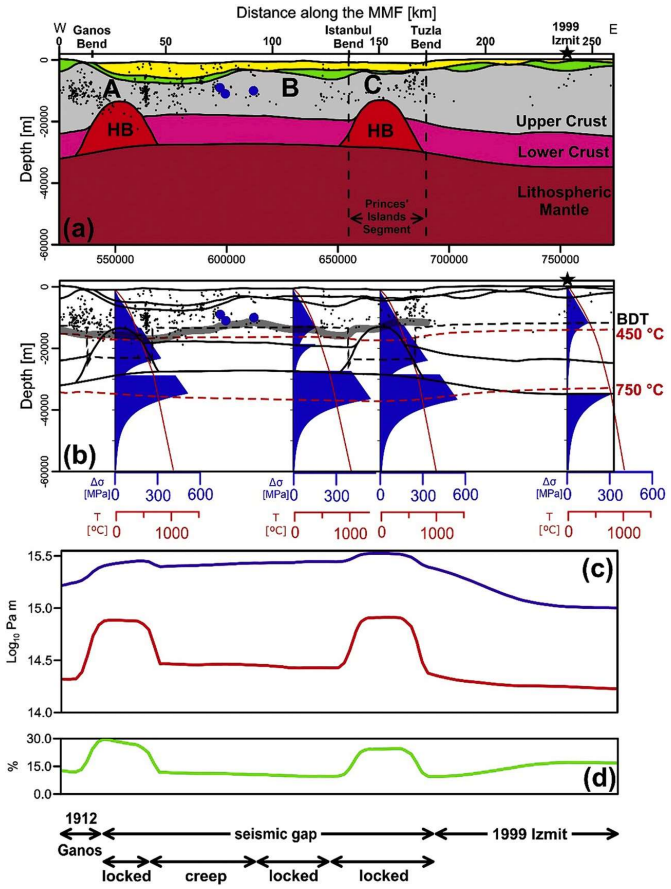

Figure 6. Cross-sections along the MMF with results and interpretation from thermal-rheological model. (a) Structural model (for details see Figs. 2 and 3). Small black dots represent observed seismicity (*Wollin et al.*, 2018) of M_w > 2.1 and in a window of ±5 km around the MMF; small blue circles represent recent seismic activity (M_w 4.4, M_w 5.7, M_w 4.1 eastward) in September 2019 (see also Fig. S2; *GEOFON Data Centre*, 1993). Locations of the observed (*Wollin et al.*, 2018) aseismic patches are also shown as A, B, and C. (b) Calculated extension YSE for four different points correlating with the locations of the observed aseismic patches, and the epicenter of the 1999 Izmit earthquake. The tick gray line represents the base of the observed (*Wollin et al.*, 2018) seismogenic layer (based on P-wave and S-wave travel-time inversions), while the black dashed line is the modeled crustal brittle-ductile transition (BDT). The modeled 450 ◦C and 750 ◦C isotherms are indicated as red dashed lines. (c) Integrated lithospheric strength in blue and integrated crustal strength in red. (d) Ratio of the integrated crustal strength to the total integrated lithospheric strength, with the interpretation of fault segmentations along the seismic gap. (For interpretation of the references to color in this figure legend, the reader is referred to the web version of this article.)

the density- geometry configuration of the high-density lower crustal bodies is under inherent uncertainty due to the non-uniqueness of potential field modeling. In this regard, geophysical datasets such as 3-D reflection seismic observations, high-resolution crustal seismic tomography, and high-resolution shipboard gravity and magnetic measurements would be required to enhance the structural model. Consequently, future thermal and rheological models should be updated based on data available in future and an associated improved structural model.

To quantify the long-term strength configuration and to obtain information on its mechanical stability, we consider the lithosphere as an overall conductive system in thermodynamic equilibrium with its present-day geological setting. We are nevertheless aware that this assumption has two major limitations: (1) computed temperatures are conservative upper-bound estimates of the temperature distribution at shallower depths as transient thermal effects due to the effects of sediment accumulation over time have been neglected; and (2) they are not representative of secondary, transient effects due to fluid circulation within permeable sedimentary units and along major fracture zones. From point 1 above, we would expect generally colder temperatures than those modeled within the syn-kinematic sediments as these relatively young sediments have been deposited over the past 4.5 Ma (Le Pichon et al., 2014, 2016) within a shallow basin that may not yet have reached thermal equilibrium. Nevertheless, we have neglected this effect based on the results of a previous study (*Ehlers*, 2005) that has demonstrated variations between 2 and 5°C Ma^{-1} that were limited to the first 4 km depth below the surface. However, this effect has little impact on our principal findings concerning the first-order characteristics of the thermal field.

The influence of active fluid circulation has far reaching implications as indicated by the mapping of episodic mantle degassing events along major fault segments and overpressure generation observed in the Sea of Marmara (*Géli et al.*, 2018), which can influence the local mechanical state. However, a proper assessment of such effects would require observations on local temperature, heat-flow and, possibly, pore-pressure variations. Such measurements are very limited across the Marmara region or they are not publicly available.

The brittle strength is temperature independent (Eq. (2)), but the corresponding brittle-ductile transition (i.e. seismogenic depth) is limited by the efficiency of viscous creep, which is highly dependent on the local temperature conditions (Eq. (3)). Accordingly, neglecting the effects of fluid circulation in our steady-state thermal modeling may have impacts on the mechanical results. While the crustal temperature below the sediments is less prone to be affected by meteoric fluids, connate fluid and other mantle/crustal-derived fluids might be deeper components in the fluid circulation that could localize along the MMF and the subsidiary faults in the area. How and to which degree these fluid circulations would influence the seismotectonic behavior of the study area is difficult to quantify. One key question here is how the porosity-permeability structure of the MMF would be influenced dynamically and if there is a feedback regarding the rheological behavior of the lithosphere beneath the Sea of Marmara. A thermo-static mechanical model, as introduced in

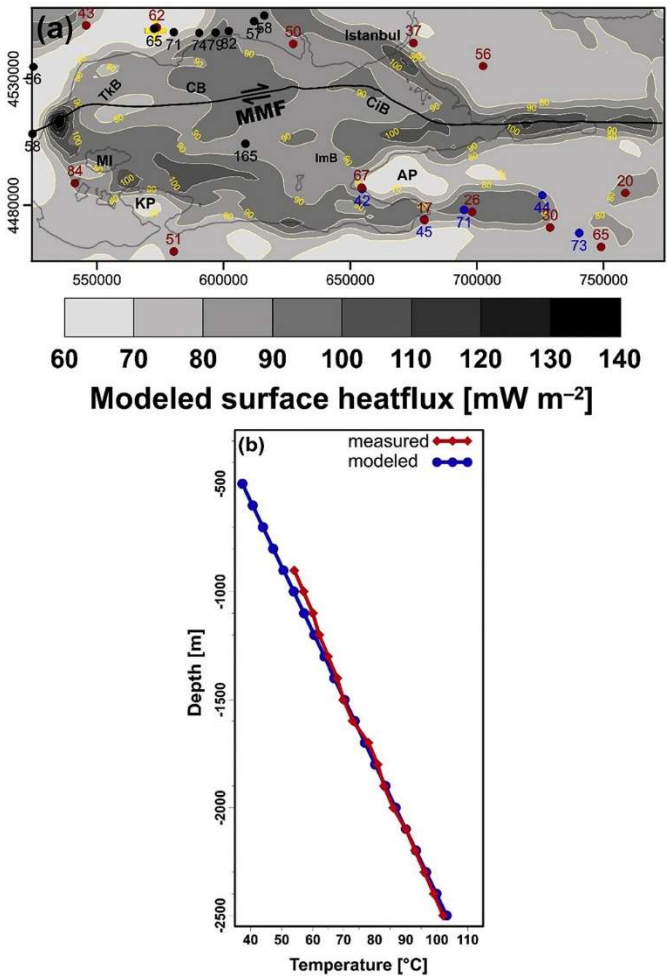

Figure 7. Thermal model versus observations. (a) Calculated surface heat-flow using a constant average value for thermal conductivity (λ = 2 mW m^{-2}). Black (*Hurtig et al.*, 1992), red (*Pfister et al.*, 1998) and blue (*Erkan*, 2015) circles are measured surface heat-flow values. (b) Observed (Pfister et al., 1998) and calculated temperature logs from the 2500-m-deep Corlu 1 well. The well location is shown as a yellow cross in (a). Abbreviations: Main Marmara Fault (MMF), Çınarcık Basin (CiB), Central Basin (CB), Tekirdag˘ Basin (TkB), Imralı Basin (ImB), Marmara Island (MI), Kapidag˘ Peninsula (KP), and Armutlu Peninsula (AP). (For interpretation of the references to colour in this figure legend, the reader is referred to the web version of this article.)

this paper, is the required first step into the investigation of the additional dynamic components in the Marmara region. However, as illustrated in Fig. 6, the modeled YSEs and related crustal brittle-ductile transition show a good fit with the observed depth characteristics of the seismogenic layer (*Wollin et al.*, 2018). In addition, previous studies have shown that the long- wavelength lithospheric temperature variations are primarily controlled by conductive heat transport (e.g., *McKenzie et al.*, 2005; *Scheck-Wenderoth et al.*, 2014). Accordingly, a conductive steady-state thermal model is a reasonable approximation to calculate the long-term rheological state of the lithosphere (e.g., *Cacace and Scheck-Wenderoth*, 2016; *Sippel et al.*, 2017; *Anikiev et al.*, 2020).

For the model area, three sets of onshore-measured surface heat-flow data exist as well as temperature measurements from a 2500-m-deep onshore well (*Hurtig et al.*, 1992; *Pfister et al.*, 1998; *Erkan*, 2015). The measured surface heat-flow is approximately 60 25 mW m^{-2} across the Marmara region (Fig. 7a).

The syn-kinematic sediment unit has the lowest assigned thermal conductivity value compared to the other geological units (Table 1). Accordingly, the modeled heat-flow values show a spatially inverse correlation with the thickness variations of the syn-kinematic sediments (Fig. 3a). As the thickness of the syn-kinematic sediments decreases, the thermal blanketing effect of the sediments also decreases, which results in higher heat-flux values. As expected, the modeled shallow thermal gradients and surface heat-flux slightly overestimate the observations. In addition to the onshore-measured surface heat-flow, there is also an offshore measurement that shows a high heat-flow value of 165 mW m^{-2} (Fig. 7a), which is almost twice as high as the modeled heat-flow (~85 mW m^{-2}) for this location. It remains unclear what the origin of this deviation could be. Apart from the trivial possibility of a measurement error, local fluid flow could explain such a high value if deep and hot fluids were rising in this region. Yet, the overall trend of the modeled surface heat-flow around the Sea of Marmara is ~70 ± 10 mW m^{-2} and thus within measurement uncertainties (mean value of 60 mW m^{-2}; Fig. 7a). Overall, temperature observations from deep wells would be a more suitable way to validate lithospheric-scale 3-D thermal models in comparison with shallow geothermal gradients and surface heat-flow (e. g., *Scheck-Wenderoth et al.*, 2014; *Sippel et al.*, 2017; *Gholamrezaie et al.*, 2018). Moreover, a good fit between observed and modeled temperatures is found within the deeper parts of the 2500-m-deep onshore well (Fig. 7b).

As we are interested in quantifying the long-term rheological configuration of the lithosphere against which the MMF has evolved, we consider secondary creep as the only active dissipation mechanism. This requires an a priori-knowledge of the background strain rate, which could be representative of the Anatolian plate. Due to the activity of the NAFZ, the actual surface strain rate is likely to vary spatially over the Marmara region, with a major concentration along the MMF, as documented by recent studies (*Le Pichon et al.*, 2003; *Flerit et al.*, 2004; *Reilinger et al.*, 2006; *Hergert and Heidbach*, 2010). However, how representative those measurements are at greater depths, is a matter of uncertainty. Given the current lack of knowledge concerning the state of stress in the crust, we therefore decided to rely on a constant strain-rate value ($\dot{\varepsilon} = 10^{-14}$ s^{-1}) over the entire modeled area. Our choice stems from the results of geodetic measurements (*Hussain et al.*, 2018), which suggest an invariance of strain rates (~0.5 microstrain yr^{-1}) during the entire inter-seismic period for the NAFZ. Accordingly, over the 250-year inter-seismic period, strain-rate values can be considered as constant, except for the first 10 years following a major earthquake (Hussain et al., 2018). Given the time interval since the last earthquake along the MMF in 1766, our assumption of a constant strain rate thus remains valid. Moreover, the estimated surface-strain value of ~0.5 microstrain yr^{-1} along the NAFZ leads to a strain-rate estimate in the range of 10^{-14} to 10^{-15} s^{-1}.

Another parameter that plays an important role in our rheological modeling is the coefficient of friction, which we used to describe crystal plasticity following Byerlee's law. In our study, we did not attempt to model any variations in the coefficient of friction, but rather imposed a constant value of 0.75 (see Methods); furthermore, we do not consider a reduction in the friction along the MMF. *Hergert and Heidbach* (2011) showed that a value of 0.05 for the coefficient of friction for the MMF is compatible with the measured slip-rate along the fault. This supports our interpretation of the MMF as a weak fault cutting through a variably strong lithosphere. In addition, *Hussain et al.* (2018) documented that for an inter-time event of 250 years (as an approximate recurrence time of the Marmara seismic gap (*Ambraseys*, 2002; *Barka et al.*, 2002; *Parsons*, 2004; *Bohnhoff et al.*, 2013, 2016a, 2017; *Murru et al.*, 2016)), average viscosities of the lower crust must be greater than 10^{20}Pa s to match the constant strain rate during the entire inter-seismic period of the NAFZ. This is in the range of magnitudes for crustal viscosities as derived from our rheological modeling (10^{20}–10^{21} Pa s, Fig. 8). Following these considerations, a weak fault zone embedded within a strong lower crust is required to reconcile the geodetic observations. Our study provides a geologically consistent explanation for such an off-fault rheological configuration that is required to match the observed strain- rate data and the recorded seismicity. Importantly, it is the presence of the mechanically strong high-density bodies in our model, which pro- vides the strong sectors around the weak MMF fault, thus limiting seismic activity within the fault domain proper. In addition, our results indicate that postseismic strain rate might not be representative to characterize the rheological crustal configuration at all spatial scales. Thus, evaluating the deep crustal structure with the type of model presented herein can be key in assessing the geomechanical behavior of large continental fault zones.

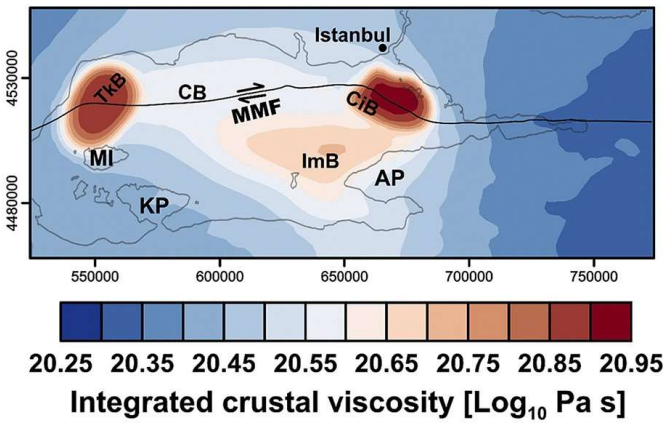

Figure 8. Integrated crustal viscosity based on the calculated average effective viscosity (see Methods, Eq. (8)) for upper crystal-line crust, lower crystalline crust and high-density bodies. Abbreviations: Main Marmara Fault (MMF), Çınarcık Basin (CiB), Central Basin (CB), Tekirdağ Basin (TkB), Imralı Basin (ImB), Marmara Island (MI), Kapidağ Peninsula (KP), and Armutlu Peninsula (AP).

Since the last two large earthquakes along the MMF occurred in September 1509 and May 1766, the recurrence time would appear to be approximately 250 years (*Ambraseys*, 2002; *Barka et al.*, 2002; *Parsons*, 2004; *Bohnhoff et al.*, 2013, 2016a, 2017; *Murru et al.*, 2016). While the extent and exact location of the rupture areas that caused these two historical events remains uncertain, there is general agreement that their magnitudes were comparable to those of recent events to the east and west, on adjacent segments of the NAFZ (~M_w 7.4). The recently published unified earthquake catalogue for the Sea of Marmara (*Wollin et al.*, 2018) covering the period between 2006 and 2016 lists 6812 events and identifies the MMF as the most seismically active segment of the NAFZ in the Marmara region. The majority of the listed events are $1.5 < M_w < 3$ and occurred at depths between 5 and 15 km (Fig. S2 in the supplementary material). Most of the seismicity occurred above the modeled depth of the 450°C isotherm. Furthermore, the seismicity distribution displays three main aseismic patches (labeled A, B and C in Fig. 6), which are considered as locked segments along the MMF and potential nucleation points for the next $M_w > 7$ Marmara earthquake (*Bohnhoff et al.*, 2013, 2017; *Wollin et al.*, 2018; *Bulut et al.*, 2019; *Lange et al.*, 2019).

Combining these observations on the character of seismicity with our thermal-rheological results (Fig. 6), the weak crystalline crustal units (i.e. the lower parts of the felsic upper crust and the ductile intermediate to mafic lower crust) extending between the two high-density bodies emerge as domains that are prone to creeping processes. The segment between the two high-density bodies is characterized by a relatively shallow brittle-ductile transitional domain (Fig. 6b) related to a more felsic composition compared to the domains of the high-density bodies. Consequently, we propose that the deeper crust along this segment of the seismic gap is a domain where seismic energy dissipation is mainly accommodated by creep. This conclusion is consistent with the interpretation by *Yamamoto et al.* (2019) based on Marmara Sea seafloor strain-rate observations in the western high that showed a steady right-lateral deformation rate of 10.7 ± 4.7 mm yr 1. Accordingly, earthquakes between the two strong lower crustal high-density bodies are likely to be relatively shallow, of low magnitude and accompanied by creep at greater depths, as observed recently in September 2019 (Fig. 6a, and Fig. S2 in the supplementary material; GEOFON Data Centre, 1993). Following a similar reasoning, we conclude that the presence of a strong crust (i.e. the high-density bodies) may explain why the MMF is locked at these locations over long-time scales. Two of the observed aseismic fault patches (A and C in Fig. 6a) correlate spatially with the locations of the modeled high-density bodies, whereas pronounced seismicity is evident at their boundaries. We interpret these areas as limiting the extent of aseismic patches of the fault, thus representing the transition between locked and creeping segments (*Bohnhoff et al.*, 2013, 2017; *Wollin et al.*, 2018). We therefore identify the mechanically strong, high-density crustal bodies as exerting the main control on the state of stress along the MMF and suggest that they are responsible for the locked state of fault segments that extend to levels below the seismogenic layer. There is, however, also an aseismic zone ("B", Fig. 6a) between the two crustal high-density bodies and beneath the central high. The sparse seismicity documented beneath this region indicates that assuming a shallow-locked sector characterized by creep at deeper crustal

levels (*Wollin et al.*, 2018; *Lange et al.*, 2019) is insufficient to explain the mechanical behavior of this segment of the fault. This implies that either aseismic creep occurs or that the fault is fully locked, as interpreted by *Lange et al.* (2019) based on seafloor strain-meter measurements. Although the modeled rheology does not provide a clear indication for a fully locked segment in this area at crustal scale, the resolved higher strength of the lithospheric mantle (Fig. 6b) in this domain could provide an explanation of why the fault is locked at lithospheric scale. *Bohnhoff et al.* (2016a) investigated the temporally and spatially distributed crustal response framing the two major seismic events in 1999, one on 17 August at Izmit (M_w 7.4, 1999a in Fig. 1b) and the second on 12 November at Düzce (M_w 7.1, 1999b in Fig. 1b). These authors identified aseismic fault patches along the rupture zones of both events and found a spatial correlation between the location of these aseismic patches and the maximum postseismic creep deformation in the ductile lower crust. The M_w 7.4 Izmit earthquake (*Barka et al.*, 2002) has been thoroughly investigated and may serve as the best reference event for evaluating the potential seismic hazard within the modeled area. This earthquake, which had a hypocentral depth between 10 and 16 km (*Barka et al.*, 2002), was the last major event in the Marmara region. The results from our modeling shows that the main hypocenter coincides with the resolved brittle-ductile transition at a depth of about 11 km (Fig. 6b), and that the lower crustal unit beneath is a rather weak ductile layer. If we compare the rheological profile beneath the Izmit earthquake epicenter (Fig. 6) with the one beneath the aseismic patch "B", it emerges that both domains share a similar rheological crustal configuration. However, the lithospheric mantle is considerably colder and rheologically stronger beneath the aseismic patch "B" under the central high compared to the Izmit area, which could explain the different deformation behavior in the two areas. Due to the presence of the two high-density bodies, the modeled lithospheric strength beneath the Princes' Island segment (Çınarcık Basin) and the Tekirdağ Basin is noticeably higher than beneath the epicenter of the 1999 Izmit event (Fig. 6b). At the locations of the two high-density bodies (correlating with the aseismic patches "A" and "C") the modeled brittle-ductile transition is at a depth of approximately 24 km. The presence of a strong crust that is mechanically coupled with the underlying mantle would imply a much stiffer lithosphere requiring significantly higher differential stresses than for the Izmit earthquake to fail. Under such a configuration, seismic failure beneath the Princes' Islands segment (or Tekirdağ Basin) would have a higher energy potential. Finally, the observed seismogenic depth along the MMF (*Wollin et al.*, 2018) ties in remarkably well with the tops of the high-density bodies in the model (Fig. 6b), again supporting the hypothesis that the MMF is locked at these locations. In addition, testing the rheological consequences of the second end-member geometry-density configuration of the high-density bodies (Model II; Fig. 2b) revealed that the presented crustal configuration for the Sea of Marmara best approximates the observed seismicity in that the top of the high-density bodies coincide with the seismogenic depth (Table S1 and Figs. S3–S8 in the supplementary material). It remains an open question how variable surface-strain rates may ultimately propagate to deeper crustal and lithosphere levels along the weak fault and beyond, and how rheological heterogeneities in the lithosphere interact with the fault zone. Our rheological model clearly indicates the presence of variations in lithospheric strength that correlate spatially with seismotectonic segments of the fault. We therefore suggest that the rheology of the crust away from the fault (high-density bodies) exerts a fundamental control on the long-term, inter-event strain within the Marmara region.

5. Conclusions

In this study, which is based on a 3-D density model of the Sea of Marmara and that integrates geological and geophysical observations, 3- D thermal and rheological models were presented. We used these models to study the lithospheric strength variations below the Sea of Marmara and the seismotectonic segmentation along the MMF. Accordingly, we conclude the following:

1. There are rheological heterogeneities in the lithosphere beneath the Marmara region. These contrasts are principally related to the crustal heterogeneities rather than the thermal anomalies within the deeper mantle.
2. Along the MMF, the lithospheric rheological variations are mainly associated with the crustal high-density bodies that spatially correlate with the two major bent segments of the fault. These bodies are mechanically stronger than the surrounding crystalline crust, and they may affect the dynamics of the MMF.
3. The rheological discontinuities along the MMF support the hypothesis that the MMF is mechanically segmented.
4. The realms of the two crustal high-density bodies may exemplify the locked segments of the MMF while the fault partially creeps between the two high-density bodies.
5. Shallow temperature measurements alone are not sufficient to constrain the deeper rheology and to predict crustal seismicity.
6. These thermal and rheological models can be used as input data for mechanical modeling of the stress field along the MMF to further investigate the segmentation hypothesis.

Credit author statement

EG and MSW designed the study. EG did the thermal and rheological modeling and discussed the results with all co-authors. EG produced the figures and wrote the paper supported by all co-authors. All co-authors contributed to the reviewing and editing of the paper.

Declaration of Competing Interest

The authors declare that they have no known competing financial interests or personal relationships that could have appeared to influence the work reported in this paper.

Acknowledgements

The research leading to these results was conducted under the auspices of the ALErT initiative (Anatolian pLateau climatE and Tectonic hazards), an Initial Training Network (ITN) financed by the European Union's Seventh Framework Programme FP7/2007–2013 under the Marie Skłodowska-Curie Actions (MSCA) REA grant agreement no. 607996 to M.S. We are thankful to Laszlo Lenkey and one anonymous reviewer for providing insightful reviews and constructive comments, which improved the quality of this paper.

Appendix A. Supplementary data

Supplementary data to this article can be found online at https://doi. org/10.1016/j.tecto.2021.228999.

References

Amante, C., Eakins, B.W., 2009. ETOPO1 1 arc-minute global relief model: procedures, data sources and analysis. In: NOAA Tech. Memo. NESDIS NGDC-24. https://doi. org/10.1594/PANGAEA.769615, 19.

Ambraseys, N., 2002. The seismic activity of the Marmara Sea Region over the last 2000 years. Bull. Seismol. Soc. Am. 92, 1–18. https://doi.org/10.1785/0120000843.

Anikiev, D., Cacace, M., Bott [Sippel], J., Gomez Dacal, M.L., Scheck-Wenderoth, M., 2020. Influence of lithosphere rheology on seismicity in an intracontinental rift: the case of the rhine graben. Front. Earth Sci. 8, 592561. https://doi.org/10.3389/ feart.2020.592561.

Armijo, R., Meyer, B., Navarro, S., King, G., Barka, A., 2002. Asymmetric slip partitioning in the sea of Marmara pull-apart: a clue to propagation processes of the North Anatolian Fault? Terra Nova 14, 80–86. https://doi.org/10.1046/j.1365- 3121.2002.00397.x.

Armijo, R., Pondard, N., Meyer, B., Ucarkus, G., De L´epinay, B.M., Malavieille, J., Dominguez, S., Gustcher, M.A., Schmidt, S., Beck, C., Cagatay, N., Cakir, Z., Imren, C., Eris, K., Natalin, B., Özalaybey, S., Tolun, L., Lefévre, I., Seeber, L., Gasperini, L., Rangin, C., Emre, O., Sarikavak, K., 2005. Submarine fault scarps in the Sea of Marmara pull-apart (North Anatolian Fault): implications for seismic hazard in Istanbul. Geochem. Geophys. Geosyst. 6. https://doi.org/10.1029/ 2004GC000896.

Barka, A., Akyüz, H.S., Altunel, E., Sunal, G., Çakir, Z., Dikbas, A., Yerli, B., Armijo, R., Meyer, B., De Chabalier, J.B., Rockwell, T., Dolan, J.R., Hartleb, R., Dawson, T., Christofferson, S., Tucker, A., Fumal, T., Langridge, R., Stenner, H., Lettis, W., Bachhuber, J., Page, W., 2002. The surface rupture and slip distribution of the 17 August 1999 Izmit earthquake (M 7.4), North Anatolian fault. Bull. Seismol. Soc. Am. 92, 43–60. https://doi.org/10.1785/0120000841.

Bayrakci, G., Laigle, M., B´ecel, A., Hirn, A., Taymaz, T., Yolsal, C., Evikbilen, S., Team, S., 2013. 3-D sediment-basement tomography of the Northern Marmara trough by a dense OBS network at the nodes of a grid of controlled source profiles along the North Anatolian fault. Geophys. J. Int. Geophys. J. Int 194, 1335–1357. https://doi. org/10.1093/gji/ggt211.

Bécel, A., Laigle, M., de Voogd, B., Hirn, A., Taymaz, T., Galvé, A., Shimamura, H., Murai, Y., Lépine, J.C., Sapin, M., Özalaybey, S., 2009. Moho, crustal architecture and deep deformation under the North Marmara Trough, from the SEISMARMARA Leg 1 offshore-onshore reflection-refraction survey. Tectonophysics 467, 1–21. https://doi.org/10.1016/j.tecto.2008.10.022.

Bécel, A., Laigle, M., de Voogd, B., Hirn, A., Taymaz, T., Yolsal-Cevikbilen, S., Shimamura, H., 2010. North Marmara Trough architecture of basin infill, basement and faults, from PSDM reflection and OBS refraction seismics. Tectonophysics 490, 1–14. https://doi.org/10.1016/j.tecto.2010.04.004.

Bohnhoff, M., Bulut, F., Dresen, G., Malin, P.E., Eken, T., Aktar, M., 2013. An earthquake gap south of Istanbul. Nat. Commun. 4, 1–6. https://doi.org/10.1038/ncomms2999.

Bohnhoff, M., Ickrath, M., Dresen, G., 2016a. Seismicity distribution in conjunction with spatiotemporal variations of coseismic slip and postseismic creep along the combined 1999 Izmit-Düzce rupture. Tectonophysics 686, 132–145. https://doi.org/ 10.1016/j.tecto.2016.07.029.

Bohnhoff, M., Martínez-Garzo´n, P., Bulut, F., Stierle, E., Ben-Zion, Y., 2016b. Maximum earthquake magnitudes along different sections of the North Anatolian fault zone. Tectonophysics. https://doi.org/10.1016/j.tecto.2016.02.028.

Bohnhoff, M., Wollin, C., Domigall, D., Küperkoch, L., Martínez-Garzón, P., Kwiatek, G., Malin, P.E., 2017. Repeating Marmara Sea earthquakes: indication for fault creep. Geophys. J. Int. Geophys. J. Int 210, 332–339. https://doi.org/10.1093/gji/ggx169.

Braun, J., Deschamps, F., Rouby, D., Dauteuil, O., 2013. Flexure of the lithosphere and the geodynamical evolution of non-cylindrical rifted passive margins: results from a numerical model incorporating variable elastic thickness, surface processes and 3D thermal subsidence. Tectonophysics 604, 72–82. https://doi.org/10.1016/j.tecto.2012.09. 033.

Bulut, F., Aktuğ, B., Yaltırak, C., Doğru, A., Özener, H., 2019. Magnitudes of future large earthquakes near Istanbul quantified from 1500 years of historical earthquakes, present-day microseismicity and GPS slip rates. Tectonophysics 764, 77–87. https:// doi.org/10.1016/j.tecto. 2019.05.005.

Burov, E.B., 2011. Rheology and strength of the lithosphere. Mar. Pet. Geol. https://doi. org/10.1016/j.marpetgeo.2011.05.008.

Burov, E.B., Watts, A.B., 2006. The long-term strength of continental lithosphere: "jelly sandwich" or "crème brûlée"? GSa ToDay GSA Today 16 doi.10.1130/1052-5173 (2006)016<4:tltSOc>2.0.cO;2.

Byerlee, J., 1978. Friction of rocks. Pure Appl. Geophys. 116, 615–626. https://doi.org/ 10.1007/BF00876528.

Cacace, M., Jacquey, A.B., 2017. Flexible parallel implicit modelling of coupled thermal–hydraulic–mechanical processes in fractured rocks. Solid Earth 8, 921–941. https://doi.org/10.5194/se-8-921-2017.

Cacace, M., Scheck-Wenderoth, M., 2016. Why intracontinental basins subside longer: 3- D feedback effects of lithospheric cooling and sedimentation on the flexural strength of the lithosphere. J. Geophys. Res. Solid Earth 121, 3742–3761. https://doi.org/10.1002/2015JB012682.

Carter, N.L., Tsenn, M.C., 1987. Flow properties of continental lithosphere. Tectonophysics 136, 27–63. https://doi.org/10.1016/0040-1951(87)90333-7.

Cermak, V., Rybach, L., 1982. Thermal conductivity and specific heat of minerals and rocks. In: Angenheister, G. (Ed.), Landolt-Börnstein, New Series, Group V, Geophysics and Space Research. Springer Berlin Heidelberg, pp. 305–343. https:// doi.org/10.1007/10201894_62.

Christensen, N.I., Mooney, W.D., 1995. Seismic velocity structure and composition of the continental crust: a global view. J. Geophys. Res. 100, 9761–

9788. https://doi.org/ 10.1029/95JB00259.
Ehlers, T.A., 2005. Crustal thermal processes and the interpretation of thermochronometer data. Rev. Mineral. Geochem. https://doi.org/10.2138/rmg.2005.58.12.
Ergintav, S., Reilinger, R.E., Çakmak, R., Floyd, M., Cakir, Z., Doıan, U., King, R.W., McClusky, S., Özener, H., 2014. Istanbul's earthquake hot spots: geodetic constraints on strain accumulation along faults in the Marmara seismic gap. Geophys. Res. Lett. 41, 5783–5788. https://doi.org/10.1002/2014GL060985.
Erkan, K., 2015. Geothermal investigations in western Anatolia using equilibrium temperatures from shallow boreholes. Solid Earth 6, 103–113. https://doi.org/ 10.5194/se-6-103-2015.
Fichtner, A., Saygin, E., Taymaz, T., Cupillard, P., Capdeville, Y., Trampert, J., 2013. The deep structure of the North Anatolian Fault Zone. Earth Planet. Sci. Lett. 373, 109–117. https://doi.org/10.1016/j.epsl.2013. 04.027.
Flerit, F., Armijo, R., King, G., Meyer, B., 2004. The mechanical interaction between the propagating North Anatolian Fault and the back-arc extension in the Aegean. Earth Planet. Sci. Lett. 224, 347–362. https://doi.org/10.1016/j.epsl.2004.05.028.
Géli, L., Henry, P., Grall, C., Tary, J.B., Lomax, A., Batsi, E., Riboulot, V., Cros, E., Gürbüz, C., Is¸ lk, S.E., Sengör, A.M.C., Le Pichon, X., Ruffine, L., Dupré, S., Thomas, Y., Kalafat, D., Bayrakci, G., Coutellier, Q., Regnier, T., Westbrook, G., Saritas, H., Çifçi, G., Çağatay, M.N., Özeren, M.S., Görür, N., Tryon, M., Bohnhoff, M., Gasperini, L., Klingelhoefer, F., Scalabrin, C., Augustin, J.M., Embriaco, D., Marinaro, G., Frugoni, F., Monna, S., Etiope, G., Favali, P., Bécel, A., 2018. Gas and seismicity within the Istanbul seismic gap. Sci. Rep. 8, 1–11. https:// doi.org/10.1038/s41598-018-23536-7.
GEOFON Data Centre, 1993. GEOFON Seismic Network [WWW Document]. Dtsch. GeoForschungsZentrum GFZ. https://doi.org/10.14470/ TR560404.
Gholamrezaie, E., Scheck-Wenderoth, M., Sippel, J., Strecker, M.R., 2018. Variability of the geothermal gradient across two differently aged magma-rich continental rifted margins of the Atlantic Ocean: the Southwest African and the Norwegian margins. Solid Earth 9, 139–158. https://doi.org/10.5194/se-9-139-2018.
Gholamrezaie, E., Scheck-Wenderoth, M., Bott, J., Heidbach, O., Strecker, M.R., 2019. 3- D crustal density model of the Sea of Marmara. Solid Earth 10, 785–807. https://doi. org/10.5194/se-10-785-2019.
Goetze, C., 1978. The mechanisms of creep in olivine. Philos. Trans. R. Soc. London. Ser. A, Math. Phys. Sci. 288, 99–119. https://doi.org/10.1098/rsta.1978.0008.
Goetze, C., Evans, B., 1979. Stress and temperature in the bending lithosphere as constrained by experimental rock mechanics. Geophys. J. Int. 59, 463–478. https:// doi.org/10.1111/j.1365-246X.1979.tb02567.x.
Henry, P., Sengör, A.C., Cagatay, M.N., 2007. MARNAUT cruise, RV L'Atalante. https:// doi.org/10.17600/7010070.
Hergert, T., Heidbach, O., 2010. Slip-rate variability and distributed deformation in the Marmara Sea fault system. Nat. Geosci. 3, 132–135. https://doi.org/10.1038/ ngeo739.
Hergert, T., Heidbach, O., 2011. Geomechanical model of the Marmara Sea region-II. 3-D contemporary background stress field. Geophys. J. Int. 185, 1090–1102. https://doi. org/10.1111/j.1365-246X.2011.04992.x.
Hergert, T., Heidbach, O., B´ecel, A., Laigle, M., 2011. Geomechanical model of the Marmara Sea region-I. 3-D contemporary kinematics. Geophys. J. Int. 185, 1073–1089. https://doi.org/10.1111/j.1365-246X.2011.04991.x.
Hurtig, E., Čermák, V., Haenel, R., Zui, V.I. (Eds.), 1992. Geothermal Atlas of Europe, set of 36 Maps and Explanatory Note, 156 pp., Hermann Haack Verlagsgesellsch., Geogr.-Kartogr. Anstalt, Gotha, Germany.
Hussain, E., Wright, T.J., Walters, R.J., Bekaert, D.P.S., Lloyd, R., Hooper, A., 2018. Constant strain accumulation rate between major earthquakes on the North Anatolian Fault. Nat. Commun. 9, 1–9. https://doi.org/10.1038/s41467-018-03739- 2.
Jackson, J., McKenzie, D., 1988. The relationship between plate motions and seismic moment tensors, and the rates of active deformation in the Mediterranean and Middle East. Geophys. J. Int. 93, 45–73. https://doi.org/10.1111/j.1365-246X.1988. tb01387.x.
Jacquey, A.B., Cacace, M., 2017. GOLEM, a MOOSE-Based Application. https://doi.org/ 10.5281/ZENODO.999401.
Karato, S.I., Wu, P., 1993. Rheology of the upper mantle: a synthesis. Science (80-.) 260, 771–778. https://doi.org/10.1126/science.260.5109.771.
Kende, J., Henry, P., Bayrakci, G., O¨ zeren, M.S., Grall, C., 2017. Moho depth and crustal thinning in the Marmara Sea region from gravity data inversion. J. Geophys. Res. Solid Earth 122, 1381–1401. https://doi.org/10.1002/2015JB012735.
Khoshmanesh, M., Shirzaei, M., 2018. Episodic creep events on the San Andreas Fault caused by pore pressure variations. Nat. Geosci. 11, 610–614. https://doi.org/ 10.1038/s41561-018-0160-2.
Laigle, M., Becel, A., de Voogd, B., Hirn, A., Taymaz, T., Ozalaybey, S., 2008. A first deep seismic survey in the Sea of Marmara: deep basins and whole crust architecture and evolution. Earth Planet. Sci. Lett. 270, 168–179. https://doi.org/10.1016/j. epsl.2008.02.031.
Lange, D., Kopp, H., Royer, J.Y., Henry, P., Çakir, Z., Petersen, F., Sakic, P., Ballu, V., Bialas, J., Özeren, M.S., Ergintav, S., Géli, L., 2019. Interseismic strain build-up on the submarine North Anatolian Fault offshore Istanbul. Nat. Commun. 10, 1–9. https://doi.org/10.1038/s41467-019-11016-z.
Le Pichon, X., Engor, A.M.C., Demirba, E., Rangin, C., Imren, C., Armijo, R., Go¨rür, N., Catay, N., Mercier de Lepinay, B., Meyer, B., Saatclar, R., Tok, B., 2001. The active Main Marmara Fault. Earth Planet. Sci. Lett. 192, 595–616. https://doi.org/ 10.1016/S0012-821X(01)00449-6.
Le Pichon, X., Chamot-Rooke, N., Rangin, C., Sengör, A.M.C., 2003. The North Anatolian fault in the Sea of Marmara. J. Geophys. Res. Solid Earth 108. https://doi.org/ 10.1029/2002jb001862.
Le Pichon, X., Imren, C., Rangin, C., Şengör, A.M.C., Siyako, M., 2014. The South Marmara Fault. Int. J. Earth Sci. 103, 219–231. https://doi.org/10.1007/s00531- 013-0950-0.
Le Pichon, X., Şengör, A.M.C., Kende, J., Imren, C., Henry, P., Grall, C., Karabulut, H., 2016. Propagation of a strike-slip plate boundary within an extensional environment: the westward propagation of the North Anatolian Fault. Can. J. Earth Sci. 53, 1416–1439. https://doi.org/10.1139/cjes-2015-0129.
Lindsey, E.O., Fialko, Y., Bock, Y., Sandwell, D.T., Bilham, R., 2014. Localized and distributed creep along the southern San Andreas Fault. J. Geophys. Res. Solid Earth 119, 7909–7922. https://doi.org/10.1002/2014JB011275.
Lockner, D.A., Morrow, C., Moore, D., Hickman, S., 2011. Low strength of deep San Andreas fault gouge from SAFOD core. Nature 472, 82–86. https://doi.org/10.1038/ nature09927.
Lorenzo-Martín, F., Roth, F., Wang, R., 2006. Elastic and inelastic triggering of earthquakes in the North Anatolian Fault zone. Tectonophysics 424, 271–289. https://doi.org/10.1016/j.tecto.2006.03.046.
McKenzie, D., Jackson, J., Priestley, K., 2005. Thermal structure of oceanic and continental lithosphere. Earth Planet. Sci. Lett. 233, 337–349. https://doi.org/ 10.1016/j.epsl.2005.02.005.
Meeßen, C., 2018. VeloDT: Fast Conversion of Upper Mantle Seismic Velocities to Density and Temperature. https://doi.org/10.5281/ZENODO.1172629.
Murru, M., Akinci, A., Falcone, G., Pucci, S., Console, R., Parsons, T., 2016. M 7 earthquake rupture forecast and time-dependent probability for the sea of Marmara region, Turkey. J. Geophys. Res. Solid Earth 121, 2679–2707. https://doi.org/ 10.1002/2015JB012595.
Parsons, T., 2004. Recalculated probability of M 7 earthquakes beneath the Sea of Marmara, Turkey. J. Geophys. Res. Solid Earth 109. https://doi.org/10.1029/ 2003JB002667.
Pfister, M., Rybach, L., Simsek, S., 1998. Geothermal reconnaissance of the Marmara Sea region (NW Turkey): surface heat flow density in an area of active continental extension. Tectonophysics 291, 77–89. https://doi.org/10.1016/S0040-1951(98)00032-8.
Priestley, K., McKenzie, D., 2006. The thermal structure of the lithosphere from shear wave velocities. Earth Planet. Sci. Lett. 244, 285–301. https://doi.org/10.1016/j. epsl.2006.01.008.

Ranalli, G., 1995. Rheology of the Earth, 2nd ed. Chapman & Hall.
Reilinger, R., McClusky, S., Vernant, P., Lawrence, S., Ergintav, S., Cakmak, R., Ozener, H., Kadirov, F., Guliev, I., Stepanyan, R., Nadariya, M., Hahubia, G., Mahmoud, S., Sakr, K., ArRajehi, A., Paradissis, D., Al-Aydrus, A., Prilepin, M., Guseva, T., Evren, E., Dmitrotsa, A., Filikov, S.V., Gomez, F., Al-Ghazzi, R., Karam, G., 2006. GPS constraints on continental deformation in the Africa-Arabia- Eurasia continental collision zone and implications for the dynamics of plate interactions. J. Geophys. Res. Solid Earth 111, B05411. https://doi.org/10.1029/2005JB004051.
Scheck-Wenderoth, M., Cacace, M., Maystrenko, Y.P., Cherubini, Y., Noack, V., Kaiser, B. O., Sippel, J., Bjo¨rn, L., 2014. Models of heat transport in the central European Basin System: effective mechanisms at different scales. Mar. Pet. Geol. 55, 315–331. https://doi.org/10.1016/j.marpetgeo.2014.03.009.
Seipold, U., 1992. Depth dependence of thermal transport properties for typical crustal rocks. Phys. Earth Planet. Inter. 69, 299–303. https://doi.org/10.1016/0031-9201 (92)90149-P.
Şengör, A.M., Tüysüz, O., Imren, C., Sakınç, M., Eyidoğan, H., Görür, N., Le Pichon, X., Rangin, C., 2005. THE NORTH ANATOLIAN FAULT: a new look. Annu. Rev. Earth Planet. Sci. 33, 37–112. https://doi.org/10.1146/annurev.earth.32.101802.120415.
Şengör, A.M.C., Grall, C., Imren, C., Le Pichon, X., Görür, N., Henry, P., Karabulut, H., Siyako, M., 2014. The geometry of the North Anatolian transform fault in the Sea of Marmara and its temporal evolution: implications for the development of intracontinental transform faults. Can. J. Earth Sci. 51, 222–242. https://doi.org/ 10.1139/cjes-2013-0160.
Sippel, J., Meeßen, C., Cacace, M., Mechie, J., Fishwick, S., Heine, C., Scheck- Wenderoth, M., Strecker, M.R., 2017. The Kenya Rift revisited: insights into lithospheric strength through data-driven 3D gravity and thermal modelling. Solid Earth 8, 45–81. https://doi.org/10.5194/se-2016-139.
Stein, R.S., Barka, A.A., Dieterich, J.H., 1997. Progressive failure on the North Anatolian fault since 1939 by earthquake stress triggering. Geophys. J. Int. 128, 594–604. https://doi.org/10.1111/j.1365-246X.1997.tb05321.x.
Sylvester, A.G., 1988. Strike-slip faults. Bull. Geol. Soc. Am. 100, 1666–1703. https:// doi.org/10.1130/0016-7606(1988)100<1666:SSF>2.3.CO;2.
Tesauro, M., Kaban, M.K., Cloetingh, S.A.P.L., 2013. Global model for the lithospheric strength and effective elastic thickness. Tectonophysics 602, 78–86. https://doi.org/ 10.1016/j.tecto.2013.01.006.
Vilà, M., Fernández, M., Jiménez-Munt, I., 2010. Radiogenic heat production variability of some common lithological groups and its significance to lithospheric thermal modeling. Tectonophysics 490, 152–164. https://doi.org/10.1016/j. tecto.2010.05.003.
Wilks, K.R., Carter, N.L., 1990. Rheology of some continental lower crustal rocks. Tectonophysics 182, 57–77. https://doi.org/10.1016/0040-1951(90)90342-6.
Wollin, C., Bohnhoff, M., Martínez-Garzón, P., Küperkoch, L., Raub, C., 2018. A unified earthquake catalogue for the Sea of Marmara Region, Turkey, based on automatized phase picking and travel-time inversion: seismotectonic implications. Tectonophysics 747–748, 416–444. https://doi.org/10.1016/j.tecto.2018.05.020.
Yaltirak, C., 2002. Tectonic evolution of the Marmara Sea and its surroundings. Mar. Geol. 190, 493–529. https://doi.org/10.1016/S0025-3227(02)00360-2.
Yamamoto, R., Kido, M., Ohta, Y., Takahashi, N., Yamamoto, Y., Pinar, A., Kalafat, D., Özener, H., Kaneda, Y., 2019. Seafloor geodesy revealed partial creep of the North
Anatolian Fault submerged in the Sea of Marmara. Geophys. Res. Lett. 46, 1268–1275. https://doi.org/10.1029/2018GL080984.
Yildirim, C., Tüysüz, O., 2017. Estimation of the long-term slip, surface uplift and block rotation along the northern strand of the North Anatolian Fault Zone: Inferences from geomorphology of the Almacık Block. Geomorphology 297, 55–68. https://doi. org/10.1016/j.geomorph.2017.08.038.